Simulations of Brownian tracer transport in squirmer suspensions

Blaise Delmotte*

Courant Institute of Mathematical Sciences, New York University, New York, NY 10012, USA
*Corresponding author: delmotte@cims.nyu.edu

Eric E. Keaveny

Department of Mathematics, Imperial College London,
South Kensington Campus, London, SW7 2AZ,UK
e.keaveny@imperial.ac.uk

AND

Eric Climent and Franck Plouraboué

Institut de Mécanique des Fluides de Toulouse (IMFT), Université de Toulouse,
CNRS-INPT-UPS, FR-31400 Toulouse, France
ecliment@imft.fr   fplourab@imft.fr

In addition to enabling movement towards environments with favourable living conditions, swimming by microorganisms has also been linked to enhanced mixing and improved nutrient uptake by their populations. Experimental studies have shown that Brownian tracer particles exhibit enhanced diffusion due to the swimmers, while theoretical models have linked this increase in diffusion to the flows generated by the swimming microorganisms, as well as collisions with the swimmers. In this study, we perform detailed simulations based on the force-coupling method and its recent extensions to the swimming and Brownian particles to examine tracer displacements and effective tracer diffusivity in squirmer suspensions. By isolating effects such as hydrodynamic or steric interactions, we provide physical insight into experimental measurements of the tracer displacement distribution. In addition, we extend results to the semi-dilute regime where the swimmer–swimmer interactions affect tracer transport and the effective tracer diffusivity no longer scales linearly with the swimmer volume fraction.

Keywords: tracer dispersion; squirmers; active suspensions; simulations.

1. Introduction

Active suspensions of micro-swimmers such as spermatozoa (Creppy *et al.*, 2015), bacteria (Wensink *et al.*, 2012) or microalgae are common both in the natural environment, such as oceans (Durham *et al.*, 2013; Pedley & Kessler, 1992; Stocker, 2012), lakes and ponds, and within living organisms, such as the human body. Such suspensions can exhibit the formation of coherent structures or complex flow patterns (Marchetti *et al.*, 2013; Saintillan & Shelley, 2011; Wensink *et al.*, 2012) which may lead to enhanced mixing of chemicals in the surrounding fluid, the alteration of suspension rheology (López *et al.*, 2015; Rafaï *et al.*, 2010) or increased nutrient uptake. Mixing and transport of microscopic, inert particles by motile microorganisms have been a topic of recent interest as such suspensions are a prime example of out-of-equilibrium systems. The particles experience Brownian motion due to their small size and are further affected by hydrodynamic interactions and collisions with the micro-swimmers.

Enhanced particle transport in active suspensions has been observed in the presence of collective motion (Wu & Libchaber, 2000) and also in the absence of it (Kurtuldu et al., 2011). Understanding the mechanism of enhanced tracer transport can provide insight into biological processes such as predator–prey interactions and the plankton food chain (Kiørboe et al., 2014), as well as chemical signalling and quorum-sensing (Kim et al., 2016). In addition, the underlying mechanism may also provide the foundation for the design of novel biomimetic micro-fluidic devices that use similar strategies for enhanced mixing and stirring at small scales.

Generally speaking, the motion of a small particle in a suspension of micro-swimmers results from the interplay between Brownian diffusion due to thermal fluctuations and transport by the flow field induced by all the swimmers. The diffusion coefficient of the tracer, D_0, is set by the Stokes–Einstein diffusivity

$$D_0 = \frac{k_B T}{\zeta}, \tag{1.1}$$

where ζ is the friction coefficient of the tracer particle and $k_B T$ the thermal energy. The tracer particles are advected by the velocity field $u(\mathbf{x})$ which corresponds to the disturbances generated by the collection of micro-swimmers in the vicinity of the tracer. The velocity $u(\mathbf{x})$ depends highly on the magnitude and the spatial rate of decay of the disturbances, as well as the local swimmer volume fraction, ϕ_v.

As the swimmers are moving, over time, the ever-changing advection of the tracer particles results in their diffusive behaviour. In the dilute regime where $\phi_v \ll 1$, many experiments (Jepson et al., 2013; Kasyap et al., 2014; Leptos et al., 2009; Mio et al., 2011) have shown that the scaling between the tracer diffusivity, D^{act}, due to swimmer activity and swimmer volume fraction is linear

$$D^{act} = D_{eff} - D_0 = \alpha \phi_v \tag{1.2}$$

where D_{eff} is the total effective tracer diffusivity and α has the units of a diffusion coefficient. In terms of swimmer number density, n, and swimming speed, U, this can also be expressed as $D^{act} = nU\Lambda$, where nU is the 'active flux' of micro-swimmers and based on dimensional analysis Λ scales like the fourth power of the swimmer size. In the dilute limit, where swimmers move along straight paths and the interactions between tracers and swimmers are well characterized, the effective diffusion coefficient can be computed (Burkholder & Brady, 2017; Kasyap et al., 2014; Lin et al., 2011; Mio et al., 2011; Pushkin et al., 2013; Pushkin & Yeomans, 2013; Thiffeault, 2014) by averaging the displacements of a single particle due to repeated interactions with swimmers that move independently of one another. In many of these studies, the swimmers are modelled as spherical squirmers. The spherical squirmer model was first introduced by Lighthill (1952) and furthered by Blake (1971) and provides the motion and flow generated by a spherical swimmer propelled by small distortions of its surface.

Theoretical studies have shown that D^{act} can be separated into two contributions: random swimmer reorientations and the entrainment by the swimmer along the straight trajectories. In the experiments of Leptos et al. (2009), the tracer diffusion coefficient in 3D dilute suspensions of C. reinhardtii was obtained from data taken over period of 2 s. Since the reorientation time of C. reinhardtii due to phase slips between flagella is approximately 10 s (Goldstein et al., 2009), swimmer reorientation does not significantly affect the tracer diffusion. Hence, by considering entrainment only, Pushkin et al. (2013) obtained an estimate (($D_{eff} - D_0)/\phi_v \simeq 83 \mu m^2 s^{-1}$), surprisingly close to the experiments of Leptos et al. (2009) (($D_{eff} - D_0)/\phi_v \simeq 81.3 \, \mu m^2 s^{-1}$). Using a similar approach, Thiffeault (2014) showed that the distribution of tracer displacements from Leptos et al. (2009) can also be reproduced using the squirmer model. However, these two works only consider point tracers while the particles in experiments

are micron-sized beads (Kasyap *et al.*, 2014; Leptos *et al.*, 2009; Mio *et al.*, 2011; Wu & Libchaber, 2000), macromolecules or dead cells (Jepson *et al.*, 2013) with a finite size. Recent experiments (Jeanneret *et al.*, 2016) in the dilute regime have shown that the front-mounted flagella of *C. reinhardtii* can trap such micron-sized particles and generate very large displacements through direct entrainment. Such dramatic events are due to near-field interactions and are strongly related to swimmer geometry, as well as actuation mechanism.

Beyond the dilute limit, there can be a breakdown in the linear dependence of the effective diffusion coefficient on swimmer volume fraction. The departure from linearity, however, appears to depend strongly on the details of the system used for study. For example, Wu & Libchaber (2000) showed that the linear scaling holds up to $\phi_v = 10\%$ in 2D films of *E. coli*, while Kasyap *et al.* (2014) observed in a 3D bath that the linear trend breaks down for $\phi_v \geqslant 2.5\%$. As stated by Kasyap *et al.* (2014), the reason for the deviation from linearity is still unclear and 'one possibility is the occurrence of multi-bacterial effects on the tracer diffusivity.' While suspensions of bacteria are known to display large-scale collective dynamics (Dombrowski *et al.*, 2004; Wu & Libchaber, 2000) characterized by swirls and jets, the nonlinear dependence is also observed in swimmer suspensions that do not exhibit larger scale motion. For example, Kurtuldu *et al.* (2011) measured tracer displacements in a suspension of *C. reinhardtii* confined to a thin film of liquid and obtained a power law for the effective diffusivity $D_{eff}/D_0 \sim \phi_v^{3/2}$. A numerical investigation (Ishikawa *et al.*, 2010) of the semi-dilute regime using the squirmer model and Stokesian Dynamics to compute the motion of non-Brownian fluid particles yielded a linear scaling of the tracer diffusivity with volume fraction for values up to $\phi_v = 15\%$.

In this paper, we present results from simulations exploring tracer transport in dilute and semi-dilute suspensions of squirmers. In our simulations, we employ recently developed numerical tools based on the force-coupling method (FCM) (Delmotte & Keaveny, 2015; Delmotte *et al.*, 2015; Keaveny, 2014; Lomholt & Maxey, 2003; Maxey & Patel, 2001) that allow for multibody hydrodynamic interactions between active and passive particles, polydispersity in particle size, particle Brownian motion that satisfies the fluctuation–dissipation theorem and steric interactions. A description of the squirmer model and fluctuating FCM is provided in Section 2. In the dilute regime, we obtain quantitative agreement between our simulation results and the experimental results of Leptos *et al.* (2009) for the effective tracer diffusion coefficient, as well as for the tracer displacement distribution. By selectively removing the flow disturbances due to the squirming modes, we quantify the contributions of hydrodynamic and steric interactions on tracer displacements and provide insight into physical mechanisms giving rise to particular features of the tracer displacement distribution. These results are shown in Section 3.1. We extend these results to semi-dilute concentrations in Section 3.2. Here, we examine the nonlinear dependence of the effective tracer diffusion coefficient on the swimmer volume fraction, as well as characterize the distribution of tracers in the suspension. Finally, we discuss our results and future directions in Section 4.

2. Mathematical model for the simulations

In our simulations, we consider N_p squirmers dispersed in fluid containing N_t tracers giving a total number of particles $N = N_p + N_t$. All particles are spherical; however, the squirmers have radius a_{sw}, while the smaller tracers have radius a. The position of particle n is denoted by $\mathbf{Y}_n$, while its orientation is $\mathbf{p}_n$.

The dynamics of the squirmers and tracers are governed by the overdamped Langevin equations as described in Appendix A. To compute the velocities and angular velocities of all particles, we rely on the FCM (Lomholt & Maxey, 2003; Maxey & Patel, 2001) and the combination of two recent

extensions of FCM to active particles (Delmotte *et al.*, 2015) based on the steady squirmer model (Blake, 1971; Ishikawa *et al.*, 2006; Lighthill, 1952) and to Brownian suspensions (Delmotte & Keaveny, 2015; Keaveny, 2014) using concepts from fluctuating hydrodynamics. In the proceeding sections, we provide short descriptions of these methods. We refer the reader to the references above for more details.

2.1 *Deterministic motion*

In FCM, the forces that the immersed particles exert on the fluid are represented by a low-order finite force multipole expansion in the Stokes equations based on Gaussian functions. Accordingly, to compute the deterministic particle velocities and angular velocities arising from the forces on the particles and squirming, we solve for the Stokes flow

$$\nabla p - \eta \nabla^2 \mathbf{u} = \sum_{n=1}^{N} \mathbf{F}_n \Delta_n(\mathbf{x}) + \sum_{n=1}^{N_p} \mathbf{S}_n \cdot \nabla \Theta_n(\mathbf{x}) + \mathbf{G}_n \cdot \nabla \Delta_n(\mathbf{x}) + \mathbf{H}_n \nabla^2 \Theta_n(\mathbf{x}) \tag{2.1}$$

$$\nabla \cdot \mathbf{u} = 0 \tag{2.2}$$

where $\mathbf{F}_n$ is the force exerted by particle n on the fluid and $\mathbf{S}_n$ is the stresslet of particle n due to its rigidity. We note in our simulations that all particles are torque-free, i.e. $\tau_n = 0$ for all n, and we ignore the tracer stresslets due to their small size. The only forces we consider are short-range pairwise repulsive forces that represent the contact forces between particle pairs and prevent their overlap (Delmotte *et al.*, 2015).

For the squirmers, we also have the force distributions generated by the motion of their surfaces. The corresponding source values in (2.1) for squirmer n are

$$\mathbf{H}_n = -\frac{4}{3}\pi \eta a_{sw}^3 B_1 \mathbf{p}_n. \tag{2.3}$$

$$\mathbf{G}_n = \frac{4}{3}\pi \eta a_{sw}^2 \left(3\mathbf{p}_n\mathbf{p}_n - \mathbf{I}\right) B_2 \tag{2.4}$$

and each yields a flow asymptotic to

$$\mathbf{u}(\mathbf{y}_n) = -\frac{B_1}{3}\frac{a_{sw}^3}{r_n^3}\left(\mathbf{I} - 3\frac{\mathbf{y}_n\mathbf{y}_n^T}{r_n^2}\right)\mathbf{p}_n + \left(\frac{a_{sw}^4}{r_n^4} - \frac{a_{sw}^2}{r_n^2}\right)\frac{B_2}{2}\left(3\left(\frac{\mathbf{p}_n \cdot \mathbf{y}_n}{r_n}\right)^2 - 1\right)\frac{\mathbf{y}_n}{r_n}$$
$$- \frac{a_{sw}^4}{r_n^4}B_2\left(\frac{\mathbf{p}_n \cdot \mathbf{y}_n}{r_n}\right)\left(\mathbf{I} - \frac{\mathbf{y}_n\mathbf{y}_n^T}{r_n^2}\right)\mathbf{p}_n. \tag{2.5}$$

where $\mathbf{y}_n = \mathbf{x} - \mathbf{Y}_n$ and $r_n = |\mathbf{y}_n|$. The parameter B_1 is related to the swimming speed through $B_1 = 3U/2$ (Blake, 1971) and $B_2 = \beta B_1$ controls the strength and sign of the swimming stresslet, $\mathbf{G}_n$. The squirming parameter β describes the relative stresslet strength (Ishikawa *et al.*, 2006). For $\beta > 0$, the squirmer is a 'puller', bringing fluid in along $\mathbf{p}_n$ and expelling it laterally, whereas if $\beta < 0$, the squirmer is a 'pusher', expelling fluid along $\mathbf{p}_n$ and bringing it in laterally.

Finally, in (2.1), we also have the two Gaussian envelopes that are used to project the particle forces onto the fluid,

$$\Delta_n(\mathbf{x}) = \left(2\pi\sigma_{n;\Delta}^2\right)^{-3/2} e^{-|\mathbf{x}-\mathbf{Y}_n|^2/2\sigma_{n;\Delta}^2}$$

$$\Theta_n(\mathbf{x}) = \left(2\pi\sigma_{n;\Theta}^2\right)^{-3/2} e^{-|\mathbf{x}-\mathbf{Y}_n|^2/2\sigma_{n;\Theta}^2}. \tag{2.6}$$

The length scales $\sigma_{n;\Delta}$ and $\sigma_{n;\Theta}$ are related to the radius, a_n, of particle n through $\sigma_{n;\Delta} = a_n/\sqrt{\pi}$ and $\sigma_{n;\Theta} = a_n/\left(6\sqrt{\pi}\right)^{1/3}$. After solving (2.1) for $\mathbf{u}$, the velocity of each tracer is determined from

$$\mathbf{V}_n = \int \mathbf{u}\Delta_n(\mathbf{x})\, d^3\mathbf{x}, \tag{2.7}$$

while for the squirmers, the velocities, angular velocities and local rates of strain are given by

$$\mathbf{V}_n = U\mathbf{p}_n - \mathbf{W}_n + \int \mathbf{u}\Delta_n(\mathbf{x})\, d^3\mathbf{x} \tag{2.8}$$

$$\mathbf{\Omega}_n = \frac{1}{2}\int [\nabla \times \mathbf{u}]\,\Theta_n(\mathbf{x})\, d^3\mathbf{x} \tag{2.9}$$

$$\mathbf{E}_n = -\mathbf{K}_n + \frac{1}{2}\int \left[\nabla\mathbf{u} + (\nabla\mathbf{u})^T\right]\Theta_n(\mathbf{x})\, d^3\mathbf{x}. = 0 \tag{2.10}$$

where the terms $\mathbf{W}_n$ and $\mathbf{K}_n$ are included to subtract away artificial self-induced velocities and local rates of strain due to the volume integration of the squirming modes. Expressions for these terms are provided in Delmotte *et al.* (2015). The local rate of strain for each squirmer is required to be zero, $\mathbf{E}_n = 0$, giving rise to the stresslets, $\mathbf{S}_n$.

2.2 *Random motion*

To compute the random velocities and angular velocities, we consider the Stokes flow

$$\nabla p - \eta\nabla^2\tilde{\mathbf{u}} = \nabla \cdot \mathbf{P} + \sum_{n=1}^{N_p} \tilde{\mathbf{S}}_n \cdot \nabla\Theta_n(\mathbf{x})$$

$$\nabla \cdot \tilde{\mathbf{u}} = 0. \tag{2.11}$$

where $\mathbf{P}$ is a fluctuating stress driving the random fluid flow. The statistics for $\mathbf{P}$, in index notation, is given by

$$\langle P_{jl}\rangle = 0 \tag{2.12}$$

$$\langle P_{jl}(\mathbf{x}, t)P_{pq}(\mathbf{x}', t')\rangle = 2k_B T\eta \left(\delta_{jp}\delta_{lq} + \delta_{jq}\delta_{lp}\right)\delta(\mathbf{x} - \mathbf{x}')\delta(t - t') \tag{2.13}$$

where $k_B T$ is the thermal energy. Using the FCM volume averaging operators, we first enforce

$$\tilde{\mathbf{E}}_n = \frac{1}{2}\int \left[\nabla\tilde{\mathbf{u}} + (\nabla\tilde{\mathbf{u}})^T\right]\Theta_n(\mathbf{x})\, d^3\mathbf{x} = 0 \tag{2.14}$$

to obtain the values of $\tilde{\mathbf{S}}_n$ and subsequently compute

$$\tilde{\mathbf{V}}_n = \int \tilde{\mathbf{u}} \Delta_n(\mathbf{x}) \, \mathrm{d}^3\mathbf{x} \tag{2.15}$$

$$\tilde{\boldsymbol{\Omega}}_n = \frac{1}{2} \int \left[\boldsymbol{\nabla} \times \tilde{\mathbf{u}} \right] \Theta_n(\mathbf{x}) \, \mathrm{d}^3\mathbf{x}. \tag{2.16}$$

As demonstrated in Keaveny (2014), the resulting velocities and angular velocities will satisfy the fluctuation–dissipation theorem with the covariance given by the FCM approximation of the mobility matrix. We note that while we have described the computation of deterministic and random velocities separately, due to the linearity of Stokes equations, these can be combined into a single computation of the total particle velocities.

2.3   Integrating the equations of motion

While this describes how we obtain the deterministic and random motions of the particles, it remains to integrate the equations of motion while accounting for the thermal drift related to the divergence of the particle mobility matrix (see Appendix A). We accomplish this by employing the midpoint drifter–corrector (DC) time integration scheme (Delmotte & Keaveny, 2015) that inherently accounts for the drift terms without having to compute them directly. In words, the DC recovers the drift by initially advancing the particle positions to the midstep using only the random velocities determined from the fluctuating fluid flow with no stresslets for particle rigidity. At the midstep, the full computation is performed to find the deterministic velocities, as well as new random particle velocities using the same initial realization of the fluctuating stress. The result is correlated motion between the initial and midstep velocities that then can be exploited to capture the correct thermal drift. For details of the scheme, including error expansions showing explicitly that the drift is recovered, the reader is referred to Delmotte & Keaveny (2015).

2.4   Simulations parameters and set-up

In our simulations, we set our parameters to match the *C. reinhardtii* experiments of Leptos *et al.* (2009). We set the swimmer-to-tracer radius ratio to $a_{sw}/a = 5$ and set the swimming speed, and hence B_1, to match $U = 100\mu m s^{-1} = 20 a_{sw} s^{-1}$. Following Thiffeault (2014), we set $\beta = 0.5$. The simulations are carried out in a triply periodic domain with edge length $L = 23 a_{sw} = 115 a$. We selected our box size to be large relative to the displacements of the tracers, yet not so large as to become computationally prohibitive. The timescale over which we study tracer displacements is $\Delta t = 0.12 - 2s$. The largest tracer displacements that we observe over these timescales are $\Delta x \approx 30a = 6 a_{sw} = 0.26L$ which is a fraction of the box size. For the swimmers that have swimming speed $20 a_{sw} s^{-1}$, if they were to swim along straight paths, then the distance they would travel ranges from $2.4 - 40 a_{sw} = 0.1 - 1.7L$, again either a fraction or on the order of the box size. For a quantitative study of the effect of the box size on squirmer suspension dynamics, see Delmotte *et al.* (2015). The Stokes equations are solved using a Fourier spectral method with $N_g = 192$ grid points in each direction. The number of tracers is set to $N_t = 1255$, resulting in a tracer volume fraction of less than 0.34%. The number of swimmers is varied from $N_p = 12$ to 451 to examine very dilute swimmer suspensions of $\phi_v = 0.4\%$, as well as semi-dilute cases where $\phi_v = 15\%$. Finally, the thermal energy $k_B T$ is set to obtain the same distribution of tracers displacements as Leptos *et al.* (2009) in the absence of swimmers. We note that the resulting value of the diffusion $D_0 = 0.34\mu^2 s^{-1}$ is slightly higher than the value $D_0 = 0.28\mu^2 s^{-1}$, given in
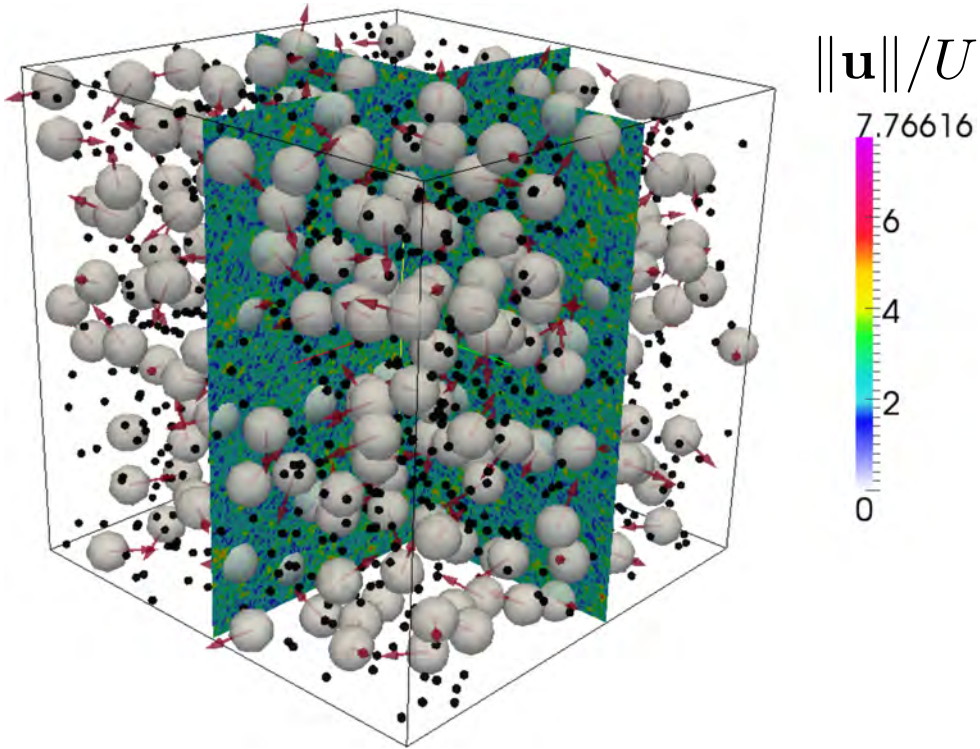
FIG. 1. Snapshot of the simulation domain containing $N_p = 301$ swimmers and 1255 tracers, with $a_{sw}/a = 5$. The volume fraction is $\phi_v = 10\%$. The large grey spheres are the squirmers and the small black dots correspond to the tracers. Vectors represent the swimmers' orientations $\mathbf{p}^n$, $n = 1, .., N_p$. The colour bar shows the norm of the fluid velocity field, $\|\mathbf{u}\|/U$, in the mid-planes. One can observe the fluid velocity fluctuations arising from the fluctuating stress.

Leptos *et al.* (2009). A snapshot taken from a representative simulation is shown in Fig. 1. It was crucial to keep the same size ratio between inert particles and swimmers. It has been shown in recent experiments (Patteson *et al.*, 2016) probing velocity perturbations in a bath of active particles that the effective diffusivity (and equivalently the effective temperature) has a non-trivial dependence on the particle size.

3. Results

3.1 *Dilute regime*

3.1.1 *Tracer displacements.* In their experiments, Leptos *et al.* (2009) measured the time-dependent probability distribution function, $P(\Delta x, \Delta t)$, for tracer displacements for suspensions with swimmer volume fractions $\phi_v = 0-2.2\%$ over 0.3 s. As the beat period for the flagella of *C. reinhardtii* is $T = 0.02$ s, this observation time corresponds to 15 beat cycles. They find that unlike previous experiments using bacterial baths (Wu & Libchaber, 2000), the tracer displacement distributions exhibit non-Gaussian tails. The non-Gaussian tails are attributed to rare entrainment events that occur when a tracer particle comes in close proximity to a swimmer's surface. We performed simulations corresponding to the same swim-

mer volume fractions and observation times as in the experiments of Leptos *et al.* (2009). The resulting tracer displacement distributions from our simulations are shown in Fig. 2(a). Our squirmer simulations adequately capture the Gaussian core of the distributions. As in Leptos *et al.* (2009), we find that the distributions are self-similar with respect to the diffusive scaling $\Delta x/(2D_{eff}\Delta t)^{1/2}$ (Fig. 2(b)). We find, however, that the larger, but rarer, displacement events related to the tails are slightly underestimated by the model. This is consistent with similar findings of tracer displacements by squirmers (Thiffeault, 2014). We attribute this to the fact that in the near-field the squirmer does not replicate the flow induced by swimming *C. reinhardtii* and the tails of the Probability Density Function (PDF) for short-time tracer
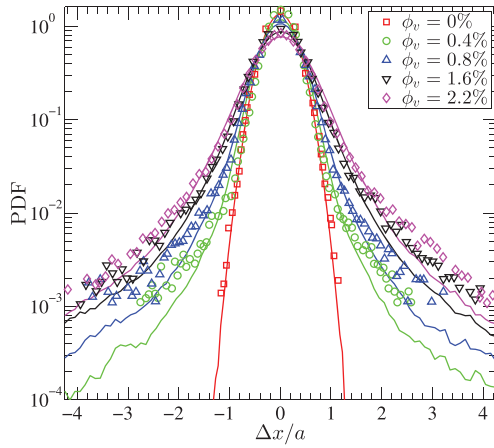
(a) PDF for tracer displacements at time $\Delta t = 0.12s$ for swimmer volume fractions $\phi_v = 0 - 2.2\%$. Symbols represent the data from Leptos *et al.* (2009). Solid lines correspond to the simulations.
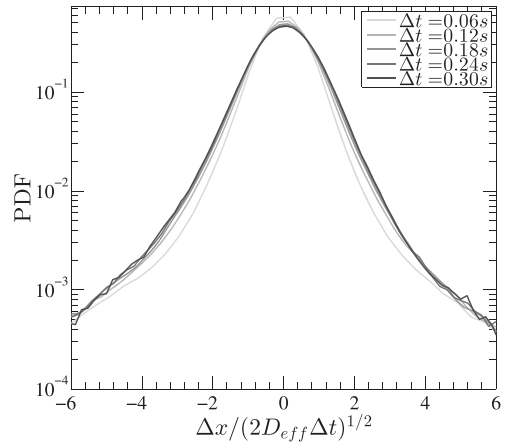
(b) Diffusive scaling of the tracer displacement PDF for $\phi_v = 2.2\%$ from the simulations
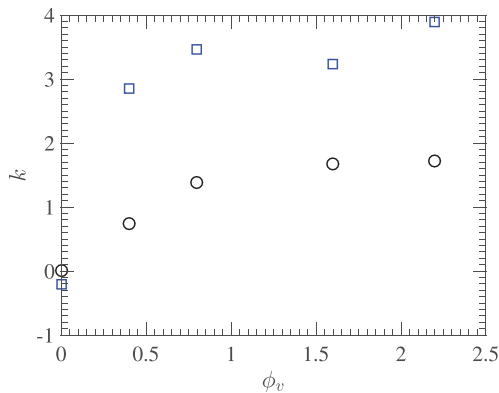
(c) Excess kurtosis k vs. ϕ_v at time $\Delta t = 0.12s$. ◯ : simulations. ☐ : calculated from the experiments of Leptos *et al.* (2009).

FIG. 2. Tracer displacements in dilute suspensions of squirmers with $\beta = 0.5$. Displacements are averaged over the three spatial directions.
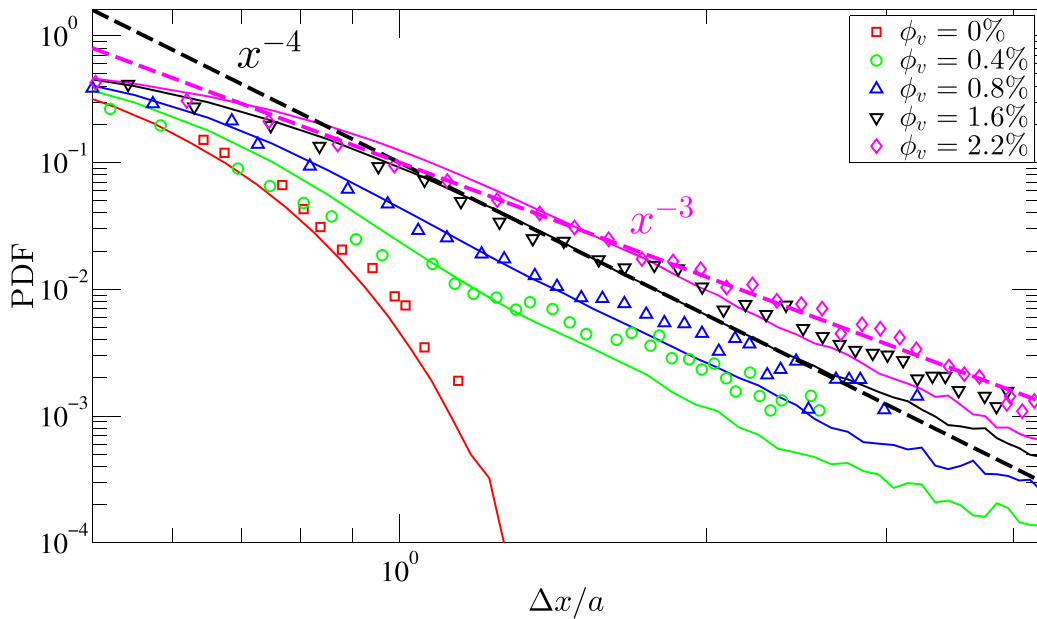
FIG. 3. The PDF of tracer displacements in log-scale. Symbols represent the data from Leptos *et al.* (2009). Solid lines correspond to the simulations. The dashed lines correspond to the power laws: ▬ ▬ ▬ ▬ : x^{-4}, ▬ ▬ ▬ ▬ : x^{-3}.

displacements depend on the details of the flow near the swimming microorganism. The differences in entrainment due to differences in swimming behaviour have been examined previously by Pushkin *et al.* (2013). In order to quantify the departure from Gaussianity and the weight of the tails, we measure the excess kurtosis of the PDF: $k = \mu_4/\mu_2^2 - 3$, where μ_k is the k-th moment of the displacement distribution. When $k = 0$, the distribution is strictly Gaussian. If $k < 0$, then the distribution has more rapidly decaying tails, while if $k > 0$, the tails decay more slowly. As shown in Fig. 2(c), the absence of swimmers yields $k = 0$ both in our simulations and in the experiments of Leptos *et al.* (2009). As ϕ_v increases, we have $k > 0$ and k increases with ϕ_v. The difference in excess kurtosis between the simulations and experiments quantifies the underestimation of the tails by the simulations.

Figure 3 shows the distribution tails in more detail. Though over less than a decade of displacements, we observe that our simulation data follow a x^{-4} power-law, while the data from Leptos *et al.* (2009) appears to behave as x^{-3}. We note that Leptos *et al.* (2009) originally fit the non-Gaussian tails by exponentials. The x^{-4} decay was observed in experiments by Kurtuldu *et al.* (2011) and predicted by Pushkin & Yeomans (2014) for suspensions of dipolar swimmers with random orientations. This prediction was obtained by combining the far-field algebraic decay of the dipolar velocity field with a random reorientation model expressed in elliptic coordinates (with the origin at the midpoint of the swimmer trajectory). The x^{-4} algebraic decay of the tracer displacement PDF, therefore, reflects the signature of the dipolar velocity field when ignoring the effect of swimmer interactions. One can observe in Fig. 3 that the slope tends to increase with ϕ_v, with the case $\phi_v = 0.4$ being closer to x^{-4} than for the subsequent cases $\phi_v = 0.8 - 2.2$. This dependence on ϕ_v indicates that the inclusion of interactions, both hydrodynamic as well as steric, alters the algebraic decay of the tracer displacement PDF, even at low values of ϕ_v.
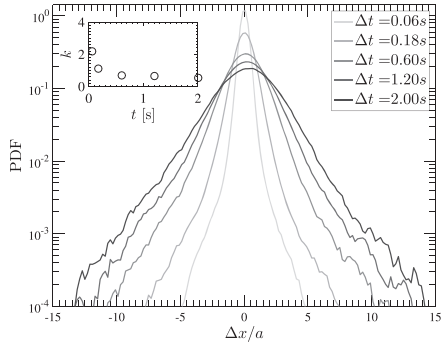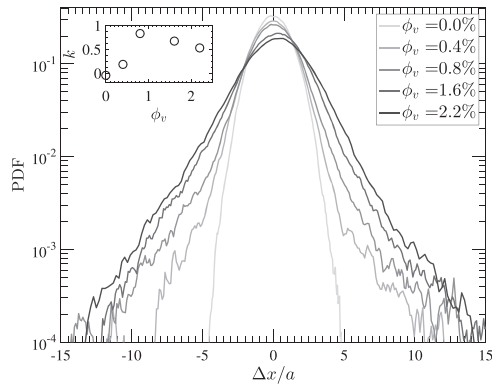
(a) PDF for tracer displacements at times $\Delta t = 0.06 - 2s$ for $\phi_v = 2.2\%$. Inset: excess kurtosis k vs. time Δt.
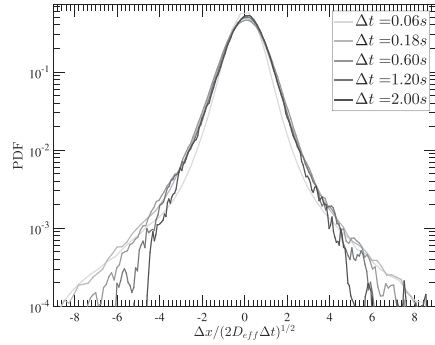
(b) Diffusive scaling of the PDF for tracer displacements for $\phi_v = 2.2\%$.

(c) PDF for tracer displacements at time $\Delta t = 2s$ for various swimmer volume fractions $\phi_v = 0 - 2.2\%$. Inset: excess kurtosis k vs. volume fraction ϕ_v.

FIG. 4. PDF of tracer displacements for long times. Displacements are averaged over the three spatial directions.

Previous studies (Thiffeault, 2014; Zaid *et al.*, 2011) have argued that the non-Gaussian tails are due to the shortness of the observation time coupled with the rarity of the entrainment events. To verify this assertion, we have computed the evolution of the tracer displacement PDF and its excess kurtosis k, over a longer time $\Delta t = 0 - 2s$ as shown in Fig. 4(a) for $\phi_v = 2.2\%$. As Δt increases, we see that the Gaussian core of the distribution broadens. We also observe that small shifts in the mean value appears, which we attribute to statistical fluctuations in the data. The convergence to a Gaussian distribution is confirmed by the decay of the excess kurtosis with Δt as shown in the inset of Fig. 4(a). After rescaling by the diffusive timescale, we see in Fig. 4(b) that the tails decay more rapidly and the distribution approaches a Gaussian as Δt increases. This convergence to a Gaussian is observed for any volume fraction $\phi_v = 0 - 2.2\%$, see Fig. 4(c). Interestingly, the excess kurtosis (inset) exhibits a non-monotonic dependence with ϕ_v, with a peak at 0.8% followed by a decay. A possible explanation for this is that for $\phi_v \leqslant 0.8\%$ there is growth in k as swimmer–tracer collisions remain infrequent, but the probability of larger displacements increases with ϕ_v. When $\phi_v > 0.8\%$, the number of encounters

(a) Mean-squared displacement over time.

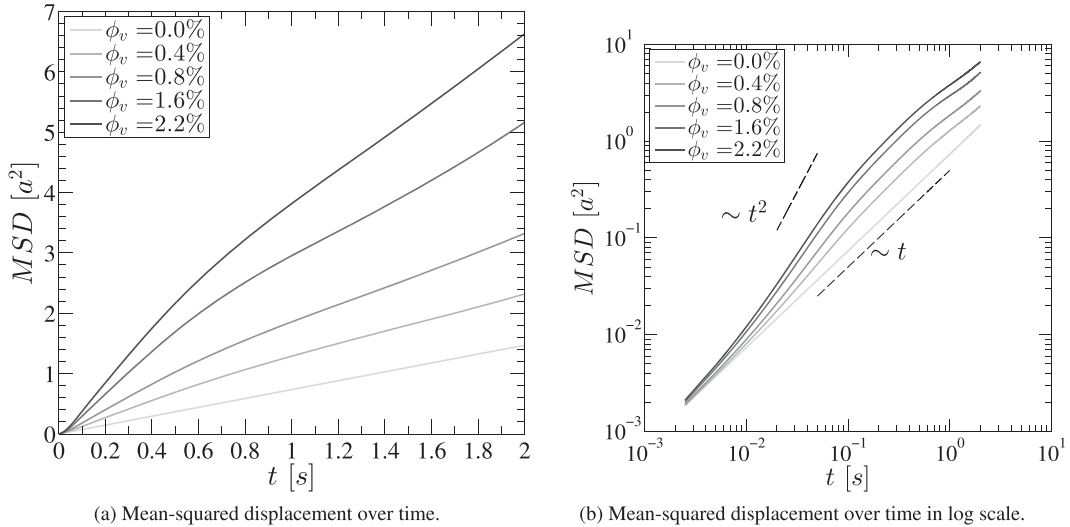(b) Mean-squared displacement over time in log scale.

FIG. 5. Mean-squared displacement of tracers for different swimmer concentrations. Displacements are averaged over the three spatial directions.

becomes sufficiently frequent as to reduce to weight of the tails and the PDF becomes more Gaussian. As we will show in Section 3.2, this decay, i.e. the rate of convergence to a Gaussian, increases with ϕ_v since collisions favour random displacements. Thiffeault (2014) derived the criterion for reaching a Gaussian distribution. He showed that for spherical squirmers with $\beta = 0.5$ the time to reach Gaussianity is $\Delta t = 3.57, 1.74, 0.8, 0.5s$ for $\phi_v = 0.4, 0.8, 1.6, 2.2\%$, respectively. Our simulation data (Fig. 4) are in accordance with these results. We also note that convergence to a Gaussian distribution in dilute suspensions was observed in experiments where the algal suspension was confined to a liquid film (Kurtuldu *et al.*, 2011).

While our results point towards convergence to a Gaussian distribution, we note that in Zaid *et al.* (2011) using point sources with no steric interactions, they found that Gaussianity should arise only when the disturbance flow induced by the swimmers decays as r^{-n} with $n = 1$, and if $n \geqslant 2$, as is the case of squirmers, the fluid velocity distribution and thus tracer displacements, should deviate from Gaussianity, even at long times. Their results are supported by the work of Rushkin *et al.* (2010) on dilute suspensions of *Volvox* ($\phi_v \leqslant 1.5\%$). Their study shows that when considering only settling forces ($n = 1$) the fluid velocity fluctuations follow a normal distribution. When accounting for the degenerate quadrupole due to ciliary beating ($n = 3$), the fluid velocity fluctuations exhibit strong deviations from Gaussianity, as confirmed by experimental data.

3.1.2 *Enhanced diffusion.* In addition to the tracer displacement distribution, Leptos *et al.* (2009) measured the mean-squared displacement of tracers as a function of time and observed that the motion of tracers is diffusive obeying $\langle \Delta x^2 \rangle = 2D_{eff}t$ for all times. Figure 5 shows the mean-squared tracer displacement from our squirmer simulations. As ϕ_v increases, we observe that the onset of the diffusive regime occurs after a period of anomalous transport at short times where $\langle \Delta x^2 \rangle \sim t^\Theta$, $1 < \Theta < 2$. We note that similar behaviour was observed in other experiments (Kurihara *et al.*, 2017; Kurtuldu *et al.*, 2011; Wu & Libchaber, 2000) and the theoretical prediction $\Theta = 3/2$ has also been proposed

(Kurihara *et al.*, 2017). Once we have reached the diffusive regime at $\Delta t = 2s$, however, our values for the mean-squared displacement are very close to those given in Leptos *et al.* (2009). We extract the effective diffusion coefficient from our data by fitting the mean-squared displacement by the solution of the Langevin equation (Wu & Libchaber, 2000)

$$\langle \Delta x^2 \rangle = 2D_{eff}\Delta t[1 - \exp(-t/\tau)] \tag{3.1}$$

where τ is the timescale over which ballistic motion $\left(\langle \Delta x^2 \rangle \sim 2\frac{D_{eff}}{\tau}t^2\right)$ transitions to diffusive behaviour $\left(\langle \Delta x^2 \rangle \sim 2D_{eff}t\right)$. In Fig. 6, we compare the effective diffusion coefficient from our simulations with those obtained by Leptos *et al.* (2009). We can see that the simulated values match the experimental ones within the statistical errors reported for the experiments.

3.1.3 *Steric versus hydrodynamic interactions.* In our simulations, and in all experiments, the tracer particles have a finite size and experience contact forces with nearby swimmers. Hence, three phenomena contribute to the tracer diffusivity in the dilute regime: the flows generated by the swimmers, collisions with swimmers due to contact forces and tracer Brownian motion. In order to quantify the effect of each, we consider three situations: (i) a bidisperse suspension of passive particles achieved by setting $U = 0, \mathbf{H}_n = \mathbf{0}$ and $\mathbf{G}_n = \mathbf{0}$ for all swimmers; (ii) a suspension where the swimmers move in the fluid without generating any swimming disturbances and interacting with the tracers through contact forces ($U \neq 0, \mathbf{H}_n = \mathbf{0}, \mathbf{G}_n = \mathbf{0}$); (iii) the full simulation model.

Figure 7 shows the resulting PDF of tracer displacements for a dilute suspension ($\phi_v = 2.2\%$) of squirmers with $\beta = 0.5$. In the purely passive case (i), the PDF is Gaussian as expected. For case (ii), the motion of the larger particles and collisions with the tracers generate a non-Gaussian PDF. The Gaussian core of this PDF is similar to that observed in case (i), but we see that there are additional non-Gaussian tails with power-law decay. When moving to the full model (case (iii)), the Gaussian core widens and the power-law decay of the tails increases. This widening of the Gaussian core was
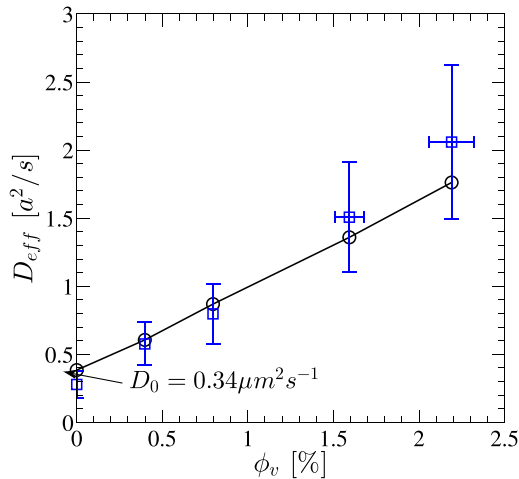

FIG. 6. Effective diffusion coefficient of tracers for the squirmer model with $\beta = 0.5$. ⌀: simulations. □: data from Leptos *et al.* (2009).
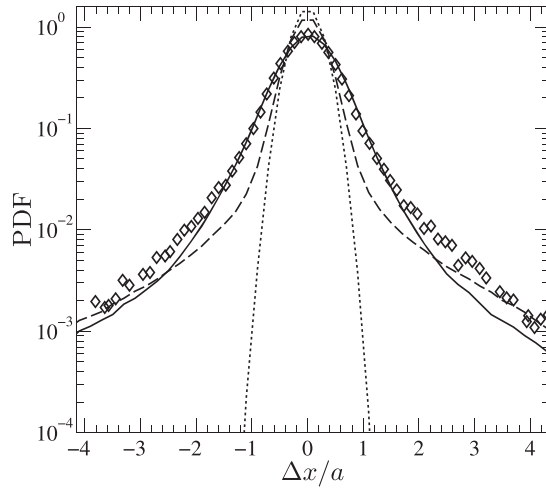
FIG. 7. PDF for tracer displacements for $\Delta t = 0.12s$ for swimmer volume fraction $\phi_v = 2.2\%$ and $\beta = 0.5$. Dotted line: case (i), swimmers replaced by passive particles, dashed line: case (ii), moving swimmers that do not generate flow, solid line: case (iii), full model, symbols: experiments from Leptos *et al.* (2009).

also seen in the experiments. These results show that rare swimmer–tracer collisions produce the large displacements that lead to the non-Gaussian tails, while the flows generated by the swimmers act to broaden the Gaussian core, thus enhancing the diffusivity of the tracer particles at short times.

3.1.4 *Role of time-dependence.* The flows generated by *C. reinhardtii* are time-dependent (Guasto *et al.*, 2010) due to the beating of its two flagella. We can include this time dependence by allowing the parameters B_1 and B_2 appearing in the steady squirmer model to be periodic functions of time. These functions can then be tuned to match the time-dependent swimming speed of *C. reinhardtii* and the location of the flow stagnation point as measured in Guasto *et al.* (2010). The details of our tuning procedure can be found in the study by Delmotte *et al.* (2015). After tuning, we find the average value of the squirming parameter over one beat period is $\bar{\beta} = 0.12$.

Figure 8 shows the PDF of tracer displacements for $\phi_v = 2.2\%$ from the fully time-dependent model. For comparison, we have also included results from simulations of the time-dependent model with $\bar{\beta} = 0.5$, as well as results from the steady model with $\beta = 0.12$ and $\beta = 0.5$. For $\beta = 0.12$, we find that the steady and time-dependent PDFs are nearly indistinguishable. As $\bar{\beta}$ increases to $\bar{\beta} = 0.5$, the PDF is slightly narrower with respect to that of its corresponding steady simulation $\beta = 0.5$. The difference, however, is quite small, and we find that time dependence of the squirming modes does not significantly affect the PDF of the tracer displacements. These results are in accordance with Dunkel *et al.* (2010) that showed in the dilute regime the time-dependent and stroke-averaged swimming disturbances provide similar tracer scattering.

3.2 *Semi-dilute regime*

In this section, we perform simulations on more concentrated suspensions using the same value for the squirming parameter $\beta = 0.5$. Figure 9 shows the time-dependent PDF for tracer displacements $P(\Delta x/a, \Delta t)$ at times $\Delta t = 0.3s$ and $\Delta t = 2s$ and for volume fractions $\phi_v = 0 - 15\%$. For all volume
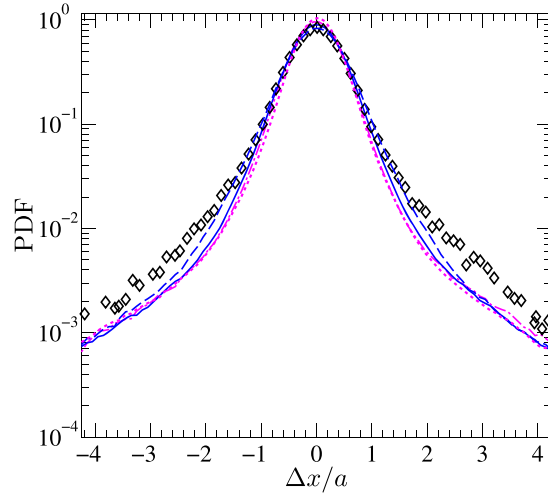
FIG. 8. PDF of tracer displacements at $\Delta t = 0.12s$ for the time-dependent and steady models with $\phi_v = 2.2\%$. $\Diamond$: data from Leptos *et al.* (2009). ———— : $\bar{\beta} = 0.5$, time-dependent. $----$: $\beta = 0.5$, steady. $-\cdot-\cdot-$: $\bar{\beta} = 0.12$, time-dependent. $\cdots\cdots$: $\beta = 0.12$, steady.

fractions, we observe that the PDF tends towards a Gaussian at long times and the excess kurtosis (insets) converges asymptotically to zero. However, the convergence rate increases with volume fraction. Using an analysis based on singular flows fields, Zaid *et al.* (2011) state that the tracer displacement distribution should only be Gaussian for $\phi_v > 25\%$ if the flows generated by the swimmers decay like r^{-n} with $n \geqslant 2$. The appearance of a Gaussian, however, agrees with the theoretical predictions of Thiffeault (2014), as well as the experimental observations of Kurtuldu *et al.* (2011) that observed an increase in Gaussianity with concentration. This, perhaps, highlights the importance of resolving the finite size of both swimmers and tracers to the observation of a Gaussian distribution of displacements. In addition,
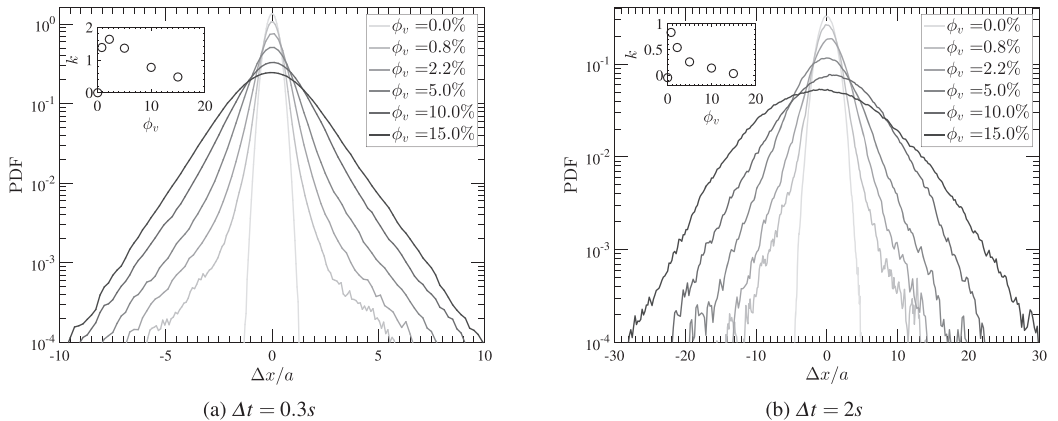

(a) $\Delta t = 0.3s$

(b) $\Delta t = 2s$

FIG. 9. PDF for tracer displacements at times $\Delta t = 0.3s$ (a), and $\Delta t = 2s$ (b), for $\phi_v = 0 - 15\%$. Inset: excess kurtosis k vs. ϕ_v.

(a) Effective diffusion coefficient of tracers. ⊖: simulations. - - - - : linear fit for the dilute regime $\phi_v = 0 - 2.2\%$. □ : data from Leptos *et al.* (2009).

(b) Mean-squared displacement of swimmers. Inset: zoom at long times to show the decrease of the slope with the concentration.
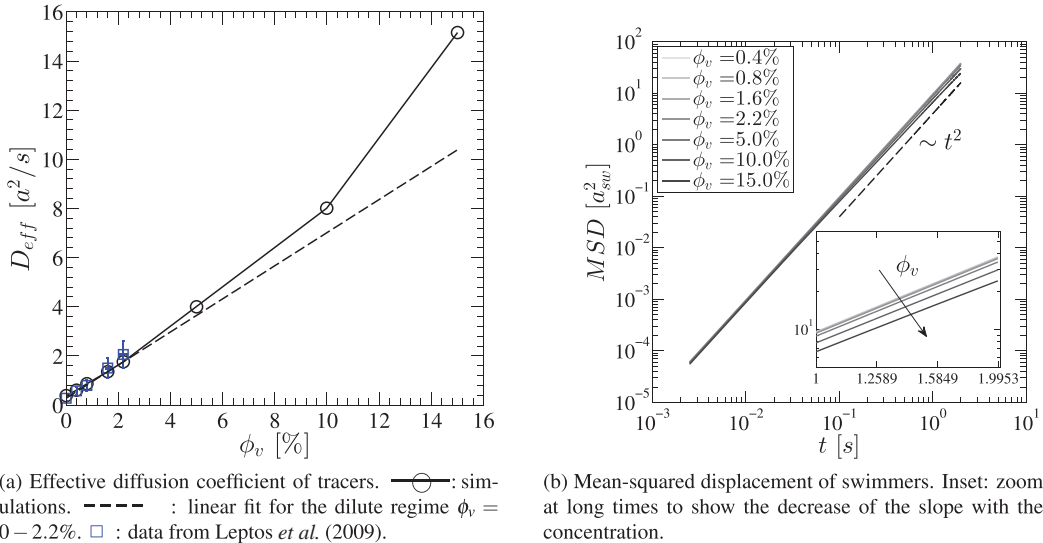
FIG. 10. Effective diffusion coefficient of tracers (a) and mean-squared displacement of swimmers (b) with $\phi_v = 0 - 15\%$.

we note a shift of the mean at long times for high-volume fraction. This is attributed to the onset of polar ordering (Delmotte *et al.*, 2015) that is typically observed in periodic squirmer suspensions.

As in the experiments of Kurtuldu *et al.* (2011) and Kasyap *et al.* (2014), our simulations show (Fig. 10(a)) the linear scaling $(D_{eff} - D_0)/\phi_v = \text{const.}$ breaks down for $\phi_v > 2.2\%$, though we do not observe a clear power law as in Kurtuldu *et al.* (2011). Additionally, our simulations yield $D_{eff}/D_0 = 11 - 22$ for $\phi_v = 5 - 10\%$, while Kurtuldu *et al.* (2011) measured $D_{eff}/D_0 \simeq 900$ for $\phi_v = 7\%$. The large difference in enhanced diffusion can be due to our simulations being 3D, while Kurtuldu *et al.* (2011) carried out experiments into a 2D film with thickness on the order of the cells' diameter ($H \simeq 15 \pm 5\mu m$), resulting in a slower decay of the flows induced by the swimming cells, as well as an increased frequency of swimmer–tracer collisions. To quantify the effect of swimmer concentration on the swimmers' motion, we examine the swimmer mean-squared displacement as a function of concentration, as shown in Fig. 10(b). While we see a slight decrease in the slope as ϕ_v increases, we observe that the swimmers are ballistic for all concentrations. Longer simulation times would be required to reach a diffusive regime in order to determine swimmer effective diffusivity $D_{eff,sw}$, as done in Ishikawa *et al.* (2010). Our simulations, therefore, correspond to a different regime than that explored in Ishikawa *et al.* (2010) where both swimmers and tracers were diffusive. We note, however, that the values $|\beta| > 1$ used in Ishikawa *et al.* (2010) are greater than the values used here to match experimental data and higher values of β do lead to the onset of diffusive behaviour for the swimmers at earlier times.

While for each concentration the swimmers' motion is ballistic, we do observe clear differences in the tracer distribution as the swimmer concentration increases. Figure 11 shows the squirmer–tracer pair distribution function $g(r, \theta)$ for $\phi_v = 2.2$ and 15%. The distribution function $g(r, \theta)$ corresponds to the likelihood, relative to a uniform distribution, of finding a tracer at a distance r from the swimmer centre of mass and with its relative position vector forming an angle θ with the swimmer orientation. At higher concentrations, there is a much higher probability of finding a tracer directly in front of the

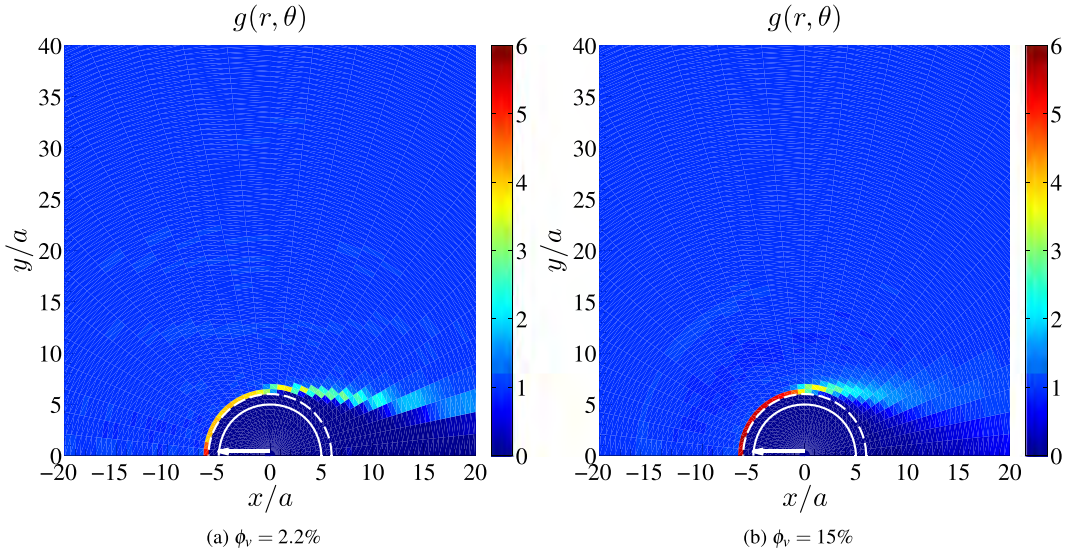(a) $\phi_v = 2.2\%$ (b) $\phi_v = 15\%$

FIG. 11. Squirmer–tracer pair distribution function $g(r,\theta)$ for $\beta = 0.5$. The white solid line represent the swimmer's radius. The white dashed line corresponds to the excluded volume region. The white arrow is the swimming direction.

swimmer, while the probability of finding tracers aft of the swimmer is reduced. This suggests that accurately representing the details of swimmer–tracer interactions for tracers directly in front of the swimmer is important in reproducing the large displacements. In addition, the increased localization of tracer particles in the vicinity of the swimmers that occurs at higher swimmer concentrations could lead to increased rates of nutrient uptake by the population.

4. Discussion and conclusion

In this study, we performed simulations of tracer motion in dilute and semi-dilute suspensions of swimming particles. Our model includes the coupled effects of the finite tracer size relative to that of the swimmers, particle Brownian motion satisfying the fluctuation–dissipation theorem and the flow disturbances induced by the swimmers using the steady squirmer model. For dilute suspensions, our simulations reproduce quantitatively the tracer displacement distribution and tracer diffusivity measured experimentally by Leptos *et al.* (2009), as well as those predicted theoretically by Thiffeault (2014). We demonstrate that the non-Gaussian tails of the tracer displacement distribution are linked to collisions between the swimmers and tracers, while the width of the Gaussian core is set by the many-body hydrodynamic interactions between the tracers and swimmers, as well as latent tracer diffusion. We also show that time dependence of the squirmer modes has little effect on the distribution. In addition, our results demonstrate that at longer observation times the number of swimmer–tracer collisions increase leading to the disappearance of the non-Gaussian power-law tails and a Gaussian tracer displacement distribution. This corresponds with the predictions of Thiffeault (2014). In the semi-dilute regime, the swimmer–tracer collision rate increases and we observe a faster convergence to a Gaussian distribution of displacements. Additionally, the simulations yield a nonlinear dependence of the effective diffusion coefficient on ϕ_v though the enhancement observed was much more modest than that measured (Kurtuldu *et al.*, 2011) in the suspensions confined to a thin film. In the nonlinear regime, we found that

at the simulation timescales, the swimmers were still behaving ballistically, but there was a notable increase in the likelihood of finding tracers directly in front of the swimmers.

A particularly interesting property of this system is the importance of near contact swimmer–tracer collisions, even in dilute systems, as they lead to rare but very large displacements. Even though the squirmer model provides a reasonable description of the far-field flow of many microorganisms, it is the near-field details that matter when resolving the collisions (Pushkin & Yeomans, 2013). Thus, at longer times when there are sufficiently many collision events, the effective tracer diffusion coefficient will be determined almost exclusively by the collisions. The details of how the organisms generate flow and possibly deform their surfaces or move their flagella are then crucial in quantifying the effective diffusion (Jeanneret *et al.*, 2016). This could have important implications in predator–prey interactions, making only certain locomotion strategies viable for particle capture. For example, a swimmer with a rigid front surface could possibly be more effective at carrying along small particles as it swims, allowing more time for them to be ingested. In addition, the importance of near-field interactions on particle diffusion may certainly impact the design of synthetic artificial swimmers or other colloidal active particles for tracer mixing in microfluidic devices. Exploring the impact of different near-field swimmer–tracer interactions for swimmers that induce the same far-field flow, as well as how heterogeneity throughout the swimmer population affect tracer transport, is an area of interest for future investigation.

In bacterial suspensions, the nonlinear dependence of the effective tracer diffusion coefficient on swimmer volume fraction has been attributed (Kasyap *et al.*, 2014) to the onset of large-scale collective motion in the suspension. In squirmer suspensions, especially at semi-dilute concentrations, the long-time dispersion properties might well be affected by polar ordering (Delmotte *et al.*, 2015), which may lead to net tracer transport along a particular axis, possibly aligned with the mean swimming direction.

Finally, it would be interesting to understand the impact of confinement on tracer diffusivity, especially with regard to the thin film experiments of Kurtuldu *et al.* (2011). Due to the stress-free boundaries, the hydrodynamic interactions are longer ranged than in bulk and may therefore enhance tracer diffusivity more than in unconfined suspensions. Additionally, we expect the swimmer–tracer collision rate to increase in confined systems which should further increase long-time tracer diffusivity. Our numerical framework can simulate thin film geometries with stress-free boundary conditions while retaining Brownian motion and hydrodynamic interactions (Delmotte & Keaveny, 2015). These simulations may provide some insight into the role of confinement and boundary conditions on tracer transport and form the basis of future studies.

References

BLAKE, J. R. (1971) A spherical envelope approach to ciliary propulsion. *J. Fluid Mech.*, **46**, 199–208.

BURKHOLDER, E. & BRADY, J. F. (2017) Tracer diffusion in active suspensions. *Phys. Rev. E*, **95**, 052605.

CREPPY, A., PRAUD, O., DRUART, X., KOHNKE, P. & PLOURABOUE, F. (2015) Turbulence of swarming sperm. *Phys. Rev. E.*, **92**, 032722.

DELMOTTE, B. & KEAVENY, E. (2015) Simulating brownian suspensions with fluctuating hydrodynamics. *J. Chem. Phys.*, **143**, 244109.

DELMOTTE, B., KEAVENY, E., PLOURABOUÉ, F. & CLIMENT, E. (2015) Large-scale simulation of steady and time-dependent active suspensions with the force-coupling method. *J. Comp. Phys.*, **302**, 524–547.

DOMBROWSKI, C., CISNEROS, L., CHATKAEW, S., GOLDSTEIN, R. E. & KESSLER, J. O. (2004) Self-concentration and large-scale coherence in bacterial dynamics. *Phys. Rev. Lett.*, **93**, 098103.

DUNKEL, J., PUTZ, V. B., ZAID, I. M. & YEOMANS, J. M. (2010) Swimmer-tracer scattering at low reynolds number. *Soft Matter*, **6**, 4268–4276.

DURHAM, W., CLIMENT, E., BARRY, M., DE LILLO, F., BOFFETTA, G., CENCINI, M. & STOCKER, R. (2013) Turbulence drives micro-scale patches of motile phytoplankton. *Nat. Commun.*, **4**. 2148.

GOLDSTEIN, R. E., POLIN, M. & TUVAL, I. (2009) Noise and synchronization in pairs of beating eukaryotic flagella. *Phys. Rev. Lett.*, **103**, 168103.

GUASTO, J. S., JOHNSON, K. A. & GOLLUB, J. (2010) Oscillatory flows induced by microorganisms swimming in two dimensions. *Phys. Rev. Lett.*, **105**, 18–21.

ISHIKAWA, T., LOCSEI, J. & PEDLEY, T. (2010) Fluid particle diffusion in a semidilute suspension of model micro-organisms. *Phys. Rev. E*, **82**, 021408.

ISHIKAWA, T., SIMMONDS, M. P. & PEDLEY, T. J. (2006) Hydrodynamic interaction of two swimming model micro-organisms. *J. Fluid Mech.*, **568**, 119–160.

JEANNERET, R., PUSHKIN, D., KANTSLER, V. & POLIN, M. (2016) Entrainment dominates the interaction of microalgae with micron-sized objects. *Nat. Commun.*, **7**, 12518.

JEPSON, A., MARTINEZ, V. A., SCHWARZ-LINEK, J., MOROZOV, A. & POON, W. C. (2013) Enhanced diffusion of nonswimmers in a three-dimensional bath of motile bacteria. *Phys. Rev. E*, **88**, 041002.

KASYAP, T., KOCH, D. L. & WU, M. (2014) Hydrodynamic tracer diffusion in suspensions of swimming bacteria. *Phys. Fluids*, **26**, 081901.

KEAVENY, E. E. (2014) Fluctuating force-coupling method for simulations of colloidal suspensions. *J. Comput. Phys.*, **269**, 61–79.

KIM, M. K., INGREMEAU, F., ZHAO, A., BASSLER, B. L. & STONE, H. A. (2016) Local and global consequences of flow on bacterial quorum sensing. *Nat. Microbiol.*, **1**, 15005.

KIØRBOE, T., JIANG, H., GONÇALVES, R. J., NIELSEN, L. T. & WADHWA, N. (2014) Flow disturbances generated by feeding and swimming zooplankton. *Proc. Natl. Acad. Sci. USA*, **111**, 11738–11743.

KURIHARA, T., ARIDOME, M., AYADE, H., ZAID, I. & MIZUNO, D. (2017) Non-gaussian limit fluctuations in active swimmer suspensions. *Phys. Rev. E*, **95**, 030601.

KURTULDU, H., GUASTO, J. S., JOHNSON, K. A. & GOLLUB, J. P. (2011) Enhancement of biomixing by swimming algal cells in two-dimensional films. *Proc. Natl. Acad. Sci. USA*, **108**, 10391–10395.

LEPTOS, K. C., GUASTO, J. S., GOLLUB, J. P., PESCI, A. I. & GOLDSTEIN, R. E. (2009) Dynamics of enhanced tracer diffusion in suspensions of swimming eukaryotic microorganisms. *Phys. Rev. Lett.*, **103**, 198103.

LIGHTHILL, M. (1952) On the squirming motion of nearly spherical deformable bodies through liquids at very small reynolds numbers. *Comm. Pure Appl. Math.*, **5**, 109–118.

LIN, Z., THIFFEAULT, J.-L. & CHILDRESS, S. (2011) Stirring by squirmers. *J. Fluid Mech.*, **669**, 167–177.

LOMHOLT, S. & MAXEY, M. (2003) Force-coupling method for particulate two-phase flow: Stokes flow. *J. Comput. Phys.*, **184**, 381–405.

LÓPEZ, H. M., GACHELIN, J., DOUARCHE, C., AURADOU, H. & CLÉMENT, E. (2015) Turning bacteria suspensions into superfluids. *Phys. Rev. Lett.*, **115**, 028301.

MARCHETTI, M. C., JOANNY, J. F., RAMASWAMY, S., LIVERPOOL, T. B., PROST, J., RAO, M. & SIMHA, R. A. (2013) Hydrodynamics of soft active matter. *Rev. Mod. Phys.*, **85**, 1143–1189.

MAXEY, M. R. & PATEL, B. K. (2001) Localized force representations for particles sedimenting in stokes fow. *Int. J. Multiphase Flow*, **27**, 1603–1626.

MIÑO, G., MALLOUK, T. E., DARNIGE, T., HOYOS, M., DAUCHET, J., DUNSTAN, J., SOTO, R., WANG, Y., ROUSSELET, A. & CLEMENT, E. (2011) Enhanced diffusion due to active swimmers at a solid surface. *Phys. Rev. Lett.*, **106**, 048102.

PATTESON, A., GOPINATH, A., PUROHITA, P. & ARRATIA, P. (2016) Particle diffusion in active fluids is non-monotonic in size. *Soft Matter*, **12**, 2365–2372.

PEDLEY, T. J. & KESSLER, J. O. (1992) Hydrodynamic phenomena in suspensions of swimming microorganisms. *Annu. Rev. Fluid Mech.*, **24**, 313–358.

PUSHKIN, D. O., SHUM, H. & YEOMANS, J. M. (2013) Fluid transport by individual microswimmers. *Int. J. Fluid Mech. Res.*, **726**, 5–25.

PUSHKIN, D. O. & YEOMANS, J. M. (2013) Fluid mixing by curved trajectories of microswimmers. *Phys. Rev. Lett.*, **111**, 188101.

PUSHKIN, D. O. & YEOMANS, J. M. (2014) Stirring by swimmers in confined microenvironments. *J. Stat. Mech. Theory Exp.*, **2014**, P04030.

RAFAÏ, S., JIBUTI, L. & PEYLA, P. (2010) Effective viscosity of microswimmer suspensions. *Phys. Rev. Lett.*, **104**, 098102.

RUSHKIN, I., KANTSLER, V. & GOLDSTEIN, R. E. (2010) Fluid velocity fluctuations in a suspension of swimming Pprotists. *Phys. Rev. Lett.*, **105**, 1–4.

SAINTILLAN, D. & SHELLEY, M. J. (2011) Emergence of coherent structures and large-scale flows in motile suspensions. *J. R. Soc. Interface*, **9**, 571–585.

STOCKER, R. (2012) Marine microbes see a sea of gradients. *Science*, **338**, 628–633.

THIFFEAULT, J.-L. (2014) Short-time distribution of particle displacements due to swimming microorganisms, *Preprint* arXiv:1408.4781.

WENSINK, H., DUNKEL, J., HEIDENREICH, S., DRESCHER, K., GOLDSTEIN, R., LOWEN, H. & YEOMANS, J. (2012) Meso-scale turbulence in living fluids. *Proc. Natl. Acad. Sci. U.S.A.*, **109**, 14308–14313.

WU, X.-L. & LIBCHABER, A. (2000) Particle diffusion in a quasi-two-dimensional bacterial bath. *Phys. Rev. Lett.*, **84**, 3017.

ZAID, I. M., DUNKEL, J. & YEOMANS, J. M. (2011) Lévy fluctuations and mixing in dilute suspensions of algae and bacteria. *J. Royal Soc. Interface*, **8**, 1314–1331.

Appendix A. Equations of motion

The motion of both the spherical tracers and squirmers is governed by overdamped Langevin dynamics, which may be expressed as

$$\frac{d\mathscr{Y}}{dt} = \mathscr{V}_{sq} + \mathscr{V} + \tilde{\mathscr{V}} + k_B T \nabla_{\mathscr{Y}} \cdot \mathscr{M}^{\mathscr{V}\mathscr{F}} \tag{A.1}$$

$$\frac{d\mathscr{P}}{dt} = \mathscr{Q} \left(\mathscr{W} + \mathscr{W}_{sq} + \tilde{\mathscr{W}} \right) + k_B T \left(\mathscr{Q} \, \nabla_{\mathscr{Y}} \cdot \mathscr{M}^{\mathscr{W}\mathscr{F}} - 2 \mathscr{D}^{\mathscr{W}\mathscr{T}} \mathscr{P} \right) \tag{A.2}$$

where $\mathscr{Y}$ is the $3N \times 1$ vector containing all particle positions, i.e. $[\mathbf{Y}_1^T, \mathbf{Y}_2^T, \ldots, \mathbf{Y}_N^T]^T$, while $\mathscr{P} = [\mathbf{p}_1^T, \mathbf{p}_2^T, \ldots, \mathbf{p}_N^T]^T$ is that for the particle orientations. The matrix $\mathscr{Q}$ is the block diagonal matrix whose nonzero entries are given by $\mathscr{Q}_{3n+k, 3n+l} = \varepsilon_{klm} \mathbf{p}_m^n$ for $n = 1, \ldots, N$.

The vectors $\mathscr{V}$ and $\mathscr{W}$ are the translational and angular velocities, respectively, of the particles that are related to the vector of forces, $\mathscr{F}$, and torques, $\mathscr{T}$, on the particles through

$$\begin{bmatrix} \mathscr{V} \\ \mathscr{W} \end{bmatrix} = \begin{bmatrix} \mathscr{M}^{\mathscr{VF}} & \mathscr{M}^{\mathscr{VT}} \\ \mathscr{M}^{\mathscr{WF}} & \mathscr{M}^{\mathscr{WT}} \end{bmatrix} = \mathscr{M} \begin{bmatrix} \mathscr{F} \\ \mathscr{T} \end{bmatrix} \tag{A.3}$$

where $\mathscr{M}$ is the $6N \times 6N$ low Reynolds number mobility matrix for all particles. In (A.3), we indicate explicitly the four $3N \times 3N$ submatrices relating either forces or torques with translational or angular velocities.

In addition to $\mathscr{V}$ and $\mathscr{W}$, the particles have velocities $\mathscr{V}_{sq}$ and angular velocities $\mathscr{W}_{sq}$ which encapsulate the swimming velocity, $U\mathbf{p}_n$, of each squirmer, as well as the additional velocities and angular velocities of all particles due to the flows induced by each of the first two squirming modes (Blake, 1971; Ishikawa *et al.*, 2006).

The random velocities, $\tilde{\mathscr{V}}$, and angular velocities, $\tilde{\mathscr{W}}$, obey the fluctuation–dissipation theorem and their statistics are related to the mobility matrix $\mathscr{M}$ through

$$\langle \tilde{\mathscr{V}}(t) \rangle = 0 \tag{A.4}$$

$$\langle \tilde{\mathscr{W}}(t) \rangle = 0 \tag{A.5}$$

$$\left\langle \begin{bmatrix} \tilde{\mathscr{V}}(t) \\ \tilde{\mathscr{W}}(t) \end{bmatrix} \begin{bmatrix} \tilde{\mathscr{V}}^T(t') & \tilde{\mathscr{W}}^T(t') \end{bmatrix} \right\rangle = 2k_B T \mathscr{M} \, \delta(t - t'). \tag{A.6}$$

Also appearing in the equations of motion are the thermal drift terms $k_B T \nabla_{\mathscr{Y}} \cdot \mathscr{M}^{\mathscr{VF}}$, $k_B T \mathscr{Q} \nabla_{\mathscr{Y}} \cdot \mathscr{M}^{\mathscr{WF}}$ and $-2k_B T \mathscr{D}^{\mathscr{WT}} \mathscr{P}$ that arise from taking the overdamped limit and are required to obtain particle distribution dynamics that are governed by Smoulochowski's equation. The diagonal matrix $\mathscr{D}^{\mathscr{WT}}$ has entries $\mathscr{D}_{ij}^{\mathscr{WT}} = \mathscr{M}_{ij}^{\mathscr{WT}}$ for $i = j$ and zero otherwise.